Quantum transport in graphene *p-n* junctions with moiré superlattice modulation

Jiuning Hu,[1,2,*] Albert F. Rigosi,[1,†] Ji U. Lee,[3] Hsin-Yen Lee,[1,4] Yanfei Yang,[1,2] Chieh-I Liu,[1,5] Randolph E. Elmquist,[1] and David B. Newell[1]

[1]*Physical Measurement Laboratory, National Institute of Standards and Technology (NIST), Gaithersburg, Maryland 20899, USA*
[2]*Joint Quantum Institute, University of Maryland, College Park, Maryland 20742, USA*
[3]*College of Nanoscale Science and Engineering, State University of New York Polytechnic Institute, Albany, New York 12203, USA*
[4]*Theiss Research, La Jolla, California 92037, USA*
[5]*Graduate Institute of Applied Physics, National Taiwan University, Taipei 10617, Taiwan*

(Received 29 January 2018; revised manuscript received 4 April 2018; published 12 July 2018)

We present simulations of quantum transport in graphene *p-n* junctions (*pn*Js) in which moiré superlattice potentials are incorporated to demonstrate the interplay between *pn*Js and moiré superlattice potentials. It is shown that the longitudinal and Hall resistivity maps can be strongly modulated by the *pn*J profile, junction height, and moiré potentials. Device resistance measurements are subsequently performed on graphene/hexagonal-boron-nitride heterostructure samples with accurate alignment of crystallographic orientations to complement and support the simulation results.

DOI: 10.1103/PhysRevB.98.045412

I. INTRODUCTION

Graphene has been established as having unique electrical and optical properties [1–4]. In particular, the heterostructures of graphene and hexagonal boron nitride (*h*-BN) have drawn intense attention recently [5–8]. Some examples of complex and interesting physical phenomena are Hofstadter's butterfly [9–13], moiré superlattices [14–16], the quantum Hall effect (QHE) in *p-n* junctions (*pn*Js) [17–30], and Coulomb drag where *h*-BN is used as an insulating spacer layer [31–35]. These phenomena make graphene-based devices a vanguard for exploring two-dimensional physics and can additionally be applied towards electron optics [36], photodetection [37–41], and quantum Hall resistance standards [42–48].

In a magnetic field, graphene devices display quantized Hall resistance values of

$$\frac{1}{(4n+2)}\frac{h}{e^2},$$

where n is an integer, h is Planck's constant, and e is the elementary charge. The bipolar nature of graphene allows both positive and negative n for fixed magnetic fields and the fabrication of tunable *pn*Js by external gates. When both sides of a *pn*J are in the quantum Hall regime, the longitudinal resistivities across the *pn*J depend on which Landauer-Büttiker edge states equilibrate at the junction [17,49,50]. An extensive analysis of this behavior was explored in previous reports, using tunable gates to adjust the *pn*J [17–20]. The longitudinal and Hall resistivity is measured as a function of the voltages from the two gates, yielding a two-dimensional parameter space, or "map" of the resistivity.

In the past few years, *h*-BN has been widely used as an encapsulation and supporting material to protect and enhance the quality of graphene and other van der Waals materials [5,6,10,51]. A moiré pattern can form when graphene and *h*-BN are stacked and electron transport in graphene can be modulated by the moiré pattern potential. Especially when their crystallization orientations are aligned within 1°, the moiré pattern wavelength can be larger than 10 nm, allowing the experimental observation of Hofstadter's butterfly at accessible magnetic fields [10–13], which significantly boosts the relevant theoretical studies [52–55].

II. NUMERICAL SIMULATIONS

In this work, we report several numerical simulations describing the effects of a moiré superlattice presence on quantum Hall transport in *pn*Js. We employ a tight-binding model for a two-dimensional system composed of a graphene layer with an overlaying periodic potential representative of a moiré superlattice with a 10 nm periodicity, as seen in Fig. 1(a). These models were implemented by using the KWANT package [56,57]. The moiré superlattice potential and other details of simulation settings are adapted from Ref. [13], and fully elucidated in the Supplemental Material [58]. Three sets of simulations were performed. The first simulation involved mapping out the longitudinal resistivity of a graphene device with a perfectly straight *pn*J profile and a randomized, or "rough," *pn*J profile. Both profiles are first simulated as is and then simulated with a moiré superlattice potential imposed on them. The second set of simulations explores the dependency of Hofstadter's butterfly on the height of the *pn*J energy barrier, and the third set shows the *pn*J Hall and longitudinal resistivity maps at high magnetic field. This work is complemented by supporting experimental data collected from graphene/h-BN heterostructure devices, which typically display a moiré superlattice and whose accurate crystal alignment can lead to measurable physical effects such as Hofstadter's butterfly.

*hujiuning@gmail.com
†albert.rigosi@nist.gov

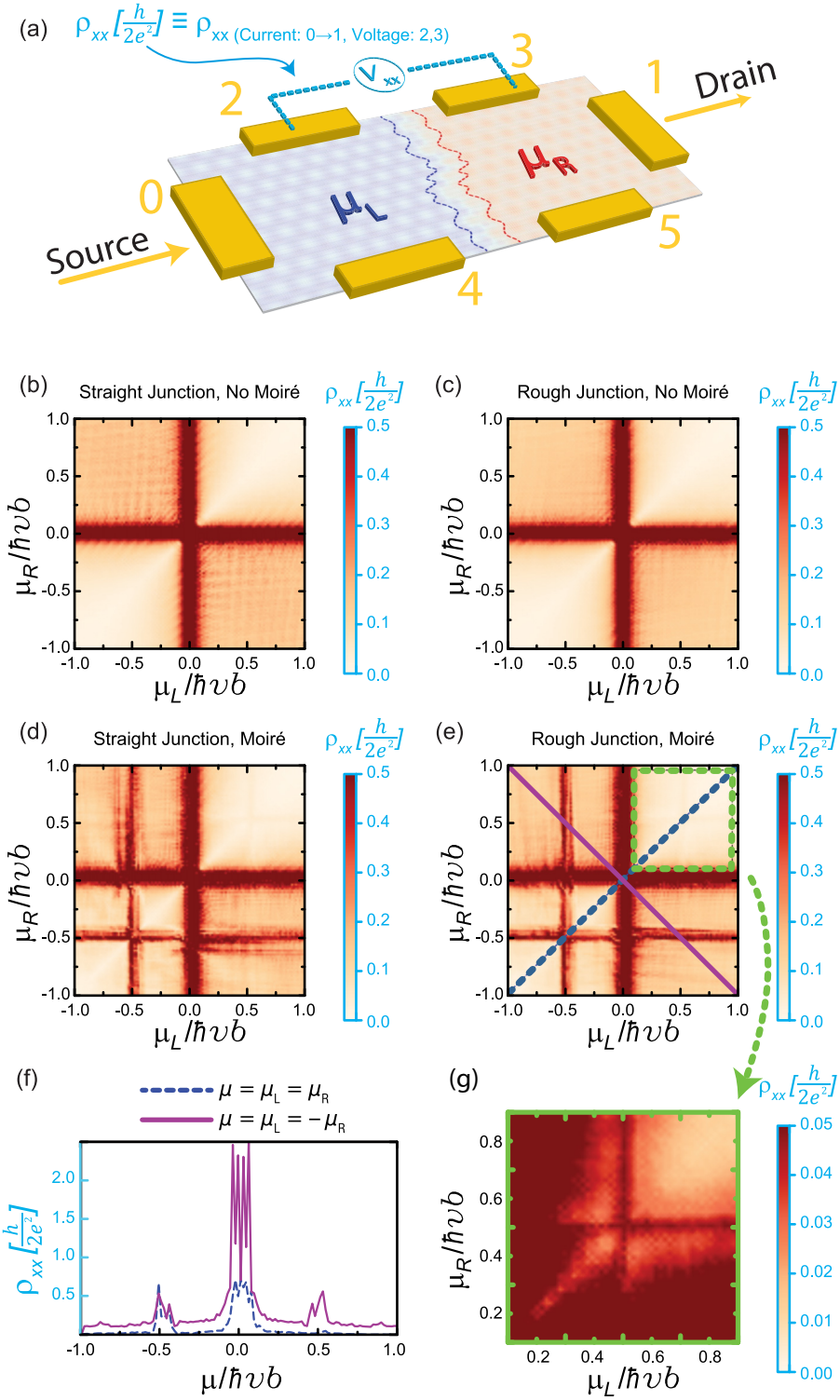

FIG. 1. (a) Illustration of graphene device with an imposed moiré superlattice potential. The chemical potentials are labeled by μ_L and μ_R and have a randomized junction profile to more accurately represent an actual device's junction roughness. The rough pnJ profile appears as a dashed blue and red line along the center of the device. (b) Longitudinal resistivity is plotted as a function of μ_L and μ_R for a straight pnJ profile. (c) The same results as in panel (b) are plotted by using a rough pnJ profile. (d) When a moiré superlattice potential is imposed, the resistivity map visibly changes in an asymmetric manner, for both the straight pnJ profile in panel (d) and for the rough pnJ profile in panel (e), with the addition of satellite Dirac peaks. (f) Taking the solid purple and dotted blue lines in panel (e), the behaviors of the longitudinal resistivity are compared. (g) A zoom-in of panel (e) shows that a satellite Dirac peak does exist in this region, albeit at a much smaller value of resistivity. All presented longitudinal resistivity color scales are in units of $h/2e^2$. For all maps, chemical potentials are in units of $\hbar v b$, where v is the Fermi velocity and b is the reciprocal superlattice constant of approximately 0.53 nm^{-1} when the alignment between graphene and h-BN is nearly zero [14].

III. RESULTS OF NUMERICAL SIMULATIONS

A. Effects of junction profile and moiré potential

Numerical simulations were performed based on the specific device design shown in Fig. 1(a). All contact terminals are labelled with a numerical digit and the chemical potentials for the left and right regions of the sample are defined as μ_L and μ_R, respectively. The chemical potentials μ_L and μ_R are generally held at different values, but in this example illustration, the left region is marked in blue and held at a lower potential than the right region, which is marked in red. The chemical potentials are smoothly changed from μ_L and μ_R in the region enclosed by the blue and red dashed curves. The junction width of 50 nm is defined to be the average distance between the red and blue dashed curves in Fig. 1(a). The rough pnJ profile such as the one shown in Fig. 1(a) reflects a more accurate representation of the junction's roughness, as inspired by data acquired from atomic force microscopy images on the real device's junctions (see the Supplemental Material [58]).

Figures 1(d) and 1(e) show the simulations of longitudinal resistivity, plotted against μ_L and μ_R. Compared with the straight pnJ profile, the rough pnJ profile clearly gives rise to weaker interference patterns beside the main [Figs. 1(b)–1(e)] and satellite [Figs. 1(d) and 1(e)] Dirac peaks.

In Figs. 1(d) and 1(e), the simulations include a moiré superlattice potential imposed on the graphene-based device, with a straight and rough pnJ profile, respectively. Clearly, extra Dirac peaks emerge at $|\mu_L|=|\mu_R| = 0.5\,\hbar vb$. Looking at the more realistic scenario presented in Fig. 1(e), we find an interesting behavior. The diagonal cut along the solid purple line gives an expected and symmetric behavior for the longitudinal resistivity, whereas the off-diagonal cut along the dark blue line gives an asymmetrical behavior, with both curves plotted in Fig. 1(f). A zoom-in of the seemingly featureless upper-right corner of Fig. 1(e) is shown in Fig. 1(g), demonstrating that the longitudinal resistivity is not strictly zero in this region, but rather has a satellite Dirac peak local maximum along $0.5\,\hbar vb = \mu_L$ and $0.5\,\hbar vb = \mu_R$, albeit at a much lower absolute resistivity. Generally, the satellite Dirac peaks arise due to expected dips in the density of states of graphene when it is subject to a superimposed, periodic potential [14,59,60]. Furthermore, the asymmetry in the resistance of those satellite Dirac peaks can be attributed to two main factors: (1) a breaking of electron-hole symmetry as a result of next-nearest-neighbor interlayer hopping and (2) the additional perturbations caused by the differences in on-site energies present in h-BN [14].

B. Hofstadter's butterfly as a function of junction height

The second set of simulations was performed to predict the behavior of Hofstadter's butterfly of the Hall and longitudinal resistivities in response to the height of the pnJ. In Fig. 2(a), an illustration depicts the rough pnJ profile while defining the barrier height t_j. In Figs. 2(b) and 2(c), Hofstadter's butterfly can be seen in the Hall and longitudinal resistivities, respectively, when plotted against average chemical potential, in units of the energy associated with Dirac electrons of wave vector b defined in Fig. 1 [11], and magnetic flux within a superlattice unit cell, in units of the magnetic flux quantum. In these two cases, the barrier height of the pnJ is zero, making an effectively homogeneous device. However, when the junction barrier height is 100 meV as in the cases of Figs. 2(d) and 2(e), the Hall resistivity map shifts to higher energy while the longitudinal resistivity map contains wider regions of the parameter space where the values are an order of magnitude higher, particularly within the region near zero energy.

Two noticeable changes can be observed with the Hall resistivity maps. As with the case in Fig. 1, an apparent asymmetry in the map appears to the left of the central parabolic feature and can be attributed to the satellite Dirac cones which form as a result of the superlattice potential and from the interlayer hopping effects mentioned earlier. Furthermore, if Fig. 2(b) is plotted on a logarithmic scale (see Supplemental Material [58]), the right satellite peak can be verified as having a significantly smaller influence on the overall Hall resistivity map than its counterpart on the left half of the graph. The corresponding longitudinal resistivity map also shows a pair of sharp satellite features, further exemplifying the asymmetry resulting from the aforementioned effects [14].

The second noticeable change is the obvious shifting of the Hall resistivity features with junction height. Since the Hall simulations are performed in the n-type region of the device, one may expect that a decrease in the potential will increase the local Fermi energy. In Fig. 2(d), the vertical, black dashed line between the large blue and red regions corresponds exactly to $\mu = t_j = 100\,\text{meV}$ (note that $\hbar vb$ is approximately 350 meV).

The trend can continue to be seen with a junction height of 200 meV in Figs. 2(f) and 2(g), where the Hall resistivity map further shifts to higher energy. The longitudinal resistivity map maintains its general appearance but becomes spread apart in parameter space, with the near-zero-energy region forming coherent and complex patterns of high resistivity at high magnetic fields.

The similar shape of the red area in Fig. 2(b) with Hall resistivity value of $h/2e^2$ appeared in Figs. 2(e) and 2(g) with a longitudinal resistivity of $h/2e^2$, a signature result of graphene pnJ [14,17,44]. This is more profound for higher pnJ barrier heights. For example, in Fig. 2(g), the two red areas are further separated along the horizontal axis and less disturbed by the complex patterns of the longitudinal resistivity.

C. Additional simulations for QHE modulations from moiré potential

The third set of simulations involves calculating the effect of a moiré superlattice potential on a rough pnJ profile at 14 T. In Fig. 3(a), the standard behavior of the Hall resistivity in the quantum Hall regime are simulated for reference. The longitudinal resistivity map in Fig. 3(b) resembles a similar map presented in Refs. [17,20], with the upper-left corner having a slightly expanded region of decreasing, step-like resistivity.

By reintroducing the moiré potential in the system, the simulations produce the responses in Figs. 3(c) and 3(d). The Hall resistivity map in Fig. 3(c) stays relatively intact on the right half of the graph, with the exception of the emerging white strips with zero Hall resistivity between the fractional values of $h/2e^2$. The left half, however, is no longer symmetrical with

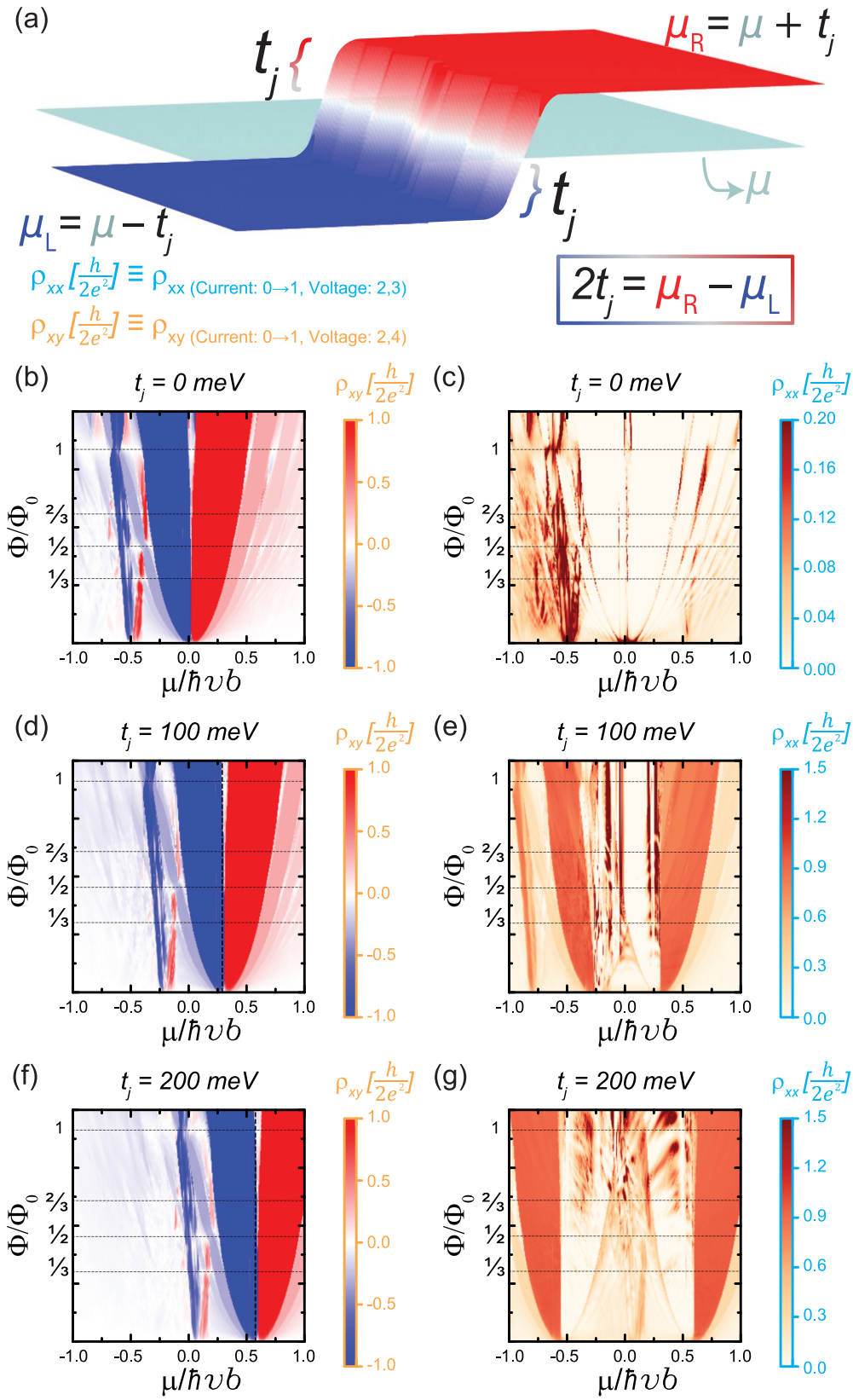

FIG. 2. (a) Illustration of a rough *pn*J profile. The barrier height t_j and the average chemical potential in the junction, μ are labeled. A moiré pattern potential was applied to the system. (b), (c) The Hall and longitudinal resistivity maps for a normal junctionless device are shown, respectively. They are plotted as a function of average chemical potential μ and the magnetic flux in units of the magnetic flux quantum Φ_0. The recursive Hofstadter's butterfly appears at the representative horizontal dashed lines at 1, 2/3, 1/2, and 1/3. This graphing style applies to the remaining resistivity maps. (d), (e) The Hall and longitudinal resistivity maps are recalculated with a 200 meV *pn*J barrier height. (f), (g) The maps are recalculated with a 400 meV *pn*J barrier height.

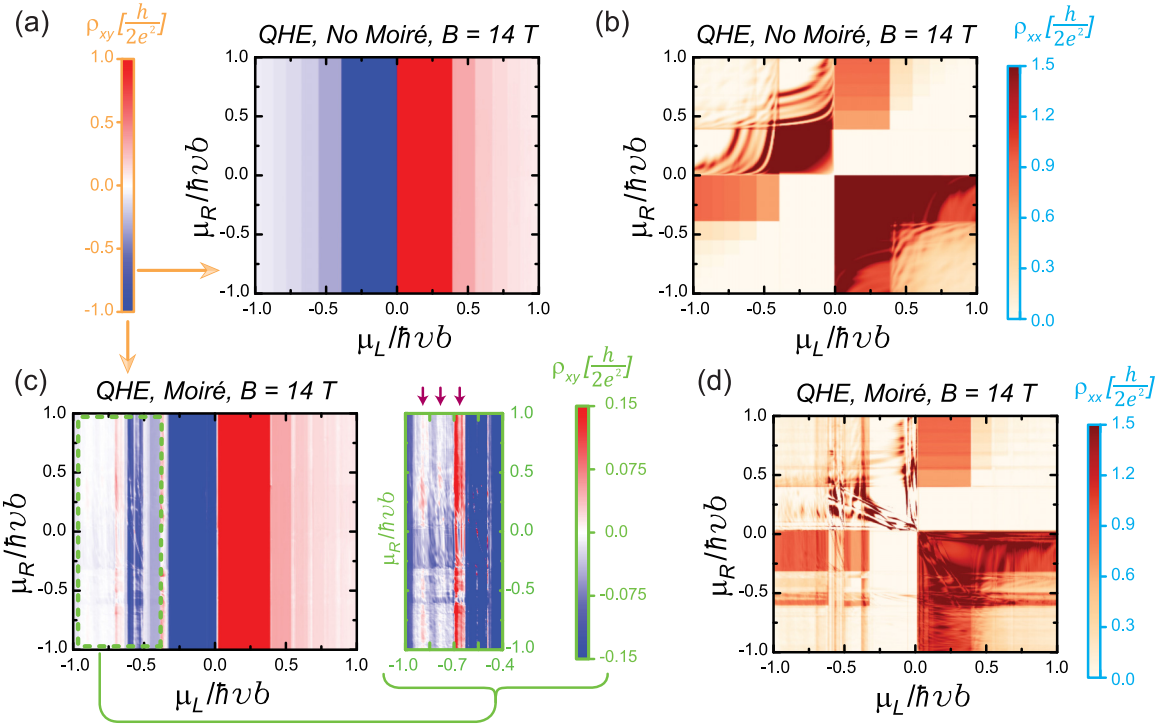

FIG. 3. (a) Hall resistivity map plotted against chemical potentials μ_L and μ_R at 14 T with no moiré potential. The red and blue colors respectively indicate positive and negative fractions of $h/2e^2$. (b) Longitudinal resistivity map for the same case as in panel (a). (c) Hall resistivity map plotted after including the effects of a moiré potential. The region within the dotted green rectangle is reproduced after an order-of-magnitude rescaling of the resistivity. (d) The longitudinal resistivity map is replotted to incorporate the effects of the moiré potential.

respect to the right half. The region in the leftmost third of the map becomes more complex, so it is rescaled to highlight the drastic changes. The most obvious change is the reversal of the sign of the resistivity, with one strong feature and two weaker features specifically at $\mu_L/\hbar v b = -0.65, -0.8, -0.9$, respectively. These sign reversals are another indication that the *h*-BN moiré potential introduces asymmetric satellite Dirac peaks whose asymmetric strengths are now to be expected. In the case of the longitudinal resistivity in Fig. 3(d), the moiré pattern potential can be seen strongly impacting the upper-left corner of the map to the extent that much of the parameter space which had a resistivity of $1.5h/2e^2$ is now zero, leaving behind the fractal-like ripples sustaining the original value. The bottom-right corner was lightly impacted in comparison, but ripples can still be observed in parts of the parameter space.

IV. EXPERIMENTAL METHODS AND RESULTS

As a proof of the basic concept, experimental results were pursued to test the numerical calculations. A heterostructure device based on graphene and *h*-BN was assembled using the flake pick-up method [51] with an orientation angle of about 1.4°, corresponding to a moiré periodicity of approximately 10 nm [61]. More information about sample fabrication can be found in the Supplemental Material [58]. In Fig. 4(a), an illustration shows the cross section of the device, containing the *h*-BN/graphene/*h*-BN sandwich atop the Si_3N_4 substrate, which has embedded tungsten gates below the surface. The separation between backgates is 50 nm. Each of the inner three gates has a width of 3 μm. The overall structural support comes from the SiO_2 and Si layers below all of the other layers. Fig. 4(b) shows an optical image of two adjacent example devices. The contact terminals and backgates are numerically labelled.

After device processing, resistance measurements were performed to gauge the validity of our numerical calculations for a system with a moiré potential of approximately the same periodicity as well as a rough, 50 nm channel *pn*J profile. One result is shown in Fig. 4(c), where longitudinal resistance data were acquired on two sets of contacts while keeping the middle and rightmost section of the device at equal chemical potentials. The longitudinal resistance curves display the satellite Dirac peaks and matched the expected asymmetrical behavior shown in Fig. 1(f). The longitudinal resistance map in Fig. 4(d) can be compared with the corresponding resistivity map in Fig. 1(e). The experimental results are in agreement with the first and more foundational set of calculations involving the moiré potential's influence on longitudinal resistivity. A faint cross can also be seen in the upper right corner of the map. The two maps' trends are identical, giving supporting evidence for the basis of the presented numerical calculations.

V. CONCLUSIONS

In conclusion, we reported several numerical simulations that incorporate moiré superlattice potentials into graphene *pn*Js so that effects on quantum transport behaviors could

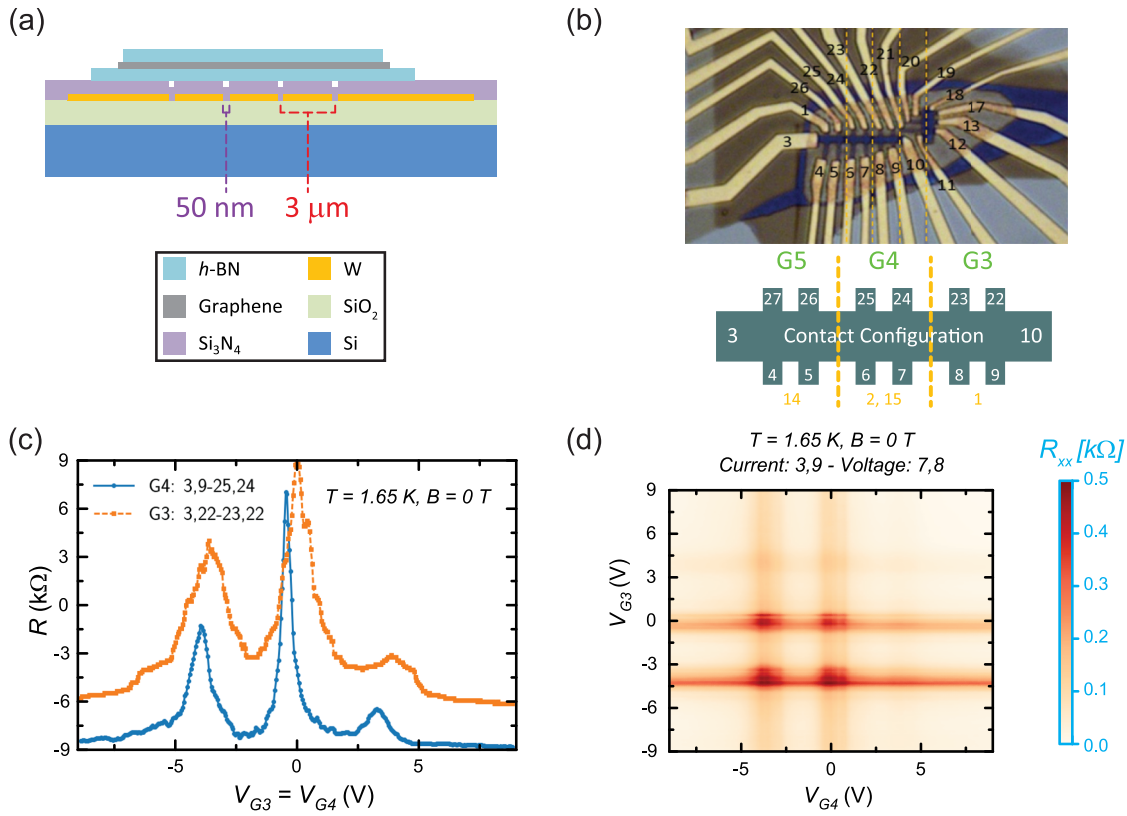

FIG. 4. (a) Illustration of a real graphene-based device showing the cross-section of the chip and the configuration of the embedded gates. (b) Optical image of an example device along with a drawing of the contact configuration for the larger device in the center of the image. The gold text in the drawing indicates the backgate contact number. (c) The data were acquired at 1.65 K with no magnetic field and are presented for the case of equal chemical potentials on the middle and rightmost regions of the device. (d) A resistance map is acquired for the voltages between −9 and 9 V for both regions of the *pn*J, which is equivalent to modifying the chemical potential in Fig. 1(e).

be predicted for a more realistic *h*-BN/graphene/*h*-BN heterostructure device. Longitudinal and Hall resistivity maps were modulated by using various parameters, giving results on how the maps were altered by the junction profile, junction height, and moiré potentials. We also supported some of the numerical calculations with experimental data from device resistance measurements.

ACKNOWLEDGMENTS

A.F.R. would like to thank the National Research Council's Research Associateship Program for the opportunity. The authors thank J. A. Stroscio for his assistance. Work done by Y.Y. was supported by federal Grant no. 70NANB12H185. The authors declare no competing financial interest.

[1] A. K. Geim and K. S. Novoselov, Nat. Mater. **6**, 183 (2007).
[2] A. H. Castro Neto, F. Guinea, N. M. R. Peres, K. S. Novoselov, and A. K. Geim, Rev. Mod. Phys. **81**, 109 (2009).
[3] K. S. Novoselov, V. I. Fal'ko, L. Colombo, P. R. Gellert, M. G. Schwab, and K. A. Kim, Nature (London) **490**, 192 (2012).
[4] S. Das Sarma, S. Adam, E. H. Hwang, and E. Rossi, Rev. Mod. Phys. **83**, 407 (2011).
[5] A. K. Geim and I. V. Grigorieva, Nature (London) **499**, 419 (2013).
[6] K. S. Novoselov, A. Mishchenko, A. Carvalho, and A. H. Castro Neto, Science **353**, aac9439 (2016).
[7] G. J. Slotman, M. M. van Wijk, P.-L. Zhao, A. Fasolino, M. I. Katsnelson, and S. Yuan, Phys. Rev. Lett. **115**, 186801 (2015).
[8] C. R. Dean, A. F. Young, I. Meric, C. Lee, L. Wang, S. Sorgenfrei, K. Watanabe, T. Taniguchi, P. Kim, K. L. Shepard, and J. Hone, Nat. Nanotechnol. **5**, 722 (2010).
[9] D. R. Hofstadter, Phys. Rev. B **14**, 2239 (1976).
[10] C. R. Dean, L. Wang, P. Maher, C. Forsythe, F. Ghahari, Y. Gao, J. Katoch, M. Ishigami, P. Moon, M. Koshino, T. Taniguchi, K. Watanabe, K. L. Shepard, J. Hone, and P. Kim, Nature (London) **497**, 598 (2013).
[11] B. Hunt, J. D. Sanchez-Yamagishi, A. F. Young, M. Yankowitz, B. J. LeRoy, K. Watanabe, T. Taniguchi, P. Moon, M. Koshino, P. Jarillo-Herrero, and R. C. Ashoori, Science **340**, 1427 (2013).
[12] L. A. Ponomarenko, R. V. Gorbachev, G. L. Yu, D. C. Elias, R. Jalil, A. A. Patel, A. Mishchenko, A. S. Mayorov, C. R. Woods, J. R. Wallbank, M. Mucha-Kruczynksi, B. A. Piot, M. Potemski, I. V. Grigorieva, K. S. Novoselov, F. Guinea, V. I. Fal'ko, and A. K. Geim, Nature (London) **497**, 594 (2013).
[13] M. Diez, J. P. Dahlhaus, M. Wimmer, and C. W. J. Beenakker, Phys. Rev. Lett. **112**, 196602 (2014).

[14] M. Yankowitz, J. Xue, D. Cormode, J. D. Sanchez-Yamagishi, K. Watanabe, T. Taniguchi, P. Jarillo-Herrero, P. Jacquod, and B. J. LeRoy, Nat. Phys. **8**, 382 (2012).

[15] J. Xue, J. Sanchez-Yamagishi, D. Bulmash, P. Jacquod, A. Deshpande, K. Watanabe, T. Taniguchi, P. Jarillo-Herrero, and B. J. LeRoy, Nat. Mater. **10**, 282 (2011).

[16] J. R. Wallbank, M. Mucha-Kruczynski, X. Chen, and V. I. Fal'ko, Ann. Phys. **527**, 359 (2015).

[17] J. R. Williams, L. DiCarlo, and C. M. Marcus, Science **317**, 638 (2007).

[18] B. Huard, J. A. Sulpizio, N. Stander, K. Todd, B. Yang, and D. Goldhaber-Gordon, Phys. Rev. Lett. **98**, 236803 (2007).

[19] B. Özyilmaz, P. Jarillo-Herrero, D. Efetov, D. A. Abanin, L. S. Levitov, and P. Kim, Phys. Rev. Lett. **99**, 166804 (2007).

[20] N. N. Klimov, S. T. Le, J. Yan, P. Agnihotri, E. Comfort, J. U. Lee, D. B. Newell, and C. A. Richter, Phys. Rev. B **92**, 241301 (2015).

[21] S. W. LaGasse and J. U. Lee, Phys. Rev. B **94**, 165312 (2016).

[22] A. F. Young and P. Kim, Nat. Phys. **5**, 222 (2009).

[23] J. R. Williams, T. Low, M. S. Lundstom, and C. M. Marcus, Nat. Nanotechnol. **6**, 222 (2011).

[24] H. Schmidt, J. C. Rode, C. Belke, D. Smirnov, and R. J. Haug, Phys. Rev. B **88**, 075418 (2013).

[25] F. Amet, J. R. Williams, K. Watanabe, T. Taniguchi, and D. Goldhaber-Gordon, Phys. Rev. Lett. **112**, 196601 (2014).

[26] T. Taychatanapat, J. Y. Tan, Y. Yeo, K. Watanabe, T. Taniguchi, and B. Özyilmaz, Nat. Commun. **6**, 6093 (2015).

[27] P. Rickhaus, M. H. Liu, P. Makk, R. Maurand, S. Hess, S. Zihlmann, M. Weiss, K. Richter, and C. Schönenberger, Nano Lett. **15**, 5819 (2015).

[28] N. Kumada, F. D. Parmentier, H. Hibino, D. C. Glattli, and P. Roulleau, Nat. Commun. **6**, 8068 (2015).

[29] J. Lee, D. Wong, J. Velasco, Jr., J. F. Rodriguez-Nieva, S. Kahn, H.-Z. Tsai, T. Taniguchi, K. Watanabe, A. Zettl, F. Wang, L. S. Levitov, and M. F. Crommie, Nat. Phys. **12**, 1032 (2016).

[30] F. Ghahari, D. Walkup, C. Gutiérrez, J. F. Rodriguez-Nieva, Y. Zhao, J. Wyrick, F. D. Natterer, W. G. Cullen, K. Watanabe, T. Taniguchi, L. S. Levitov, N. B. Zhitenev, and J. A. Stroscio, Science **356**, 845 (2017).

[31] R. V. Gorbachev, A. K. Geim, M. I. Katsnelson, K. S. Novoselov, T. Tudorovskiy, I. V. Grigorieva, A. H. MacDonald, K. Watanabe, T. Taniguchi, and L. A. Ponomarenko, Nat. Phys. **8**, 896 (2012).

[32] S. Kim and E. Tutuc, Solid State Commun. **152**, 1283 (2012).

[33] J. I. A. Li, T. Taniguchi, K. Watanabe, J. Hone, A. Levchenko, and C. R. Dean, Phys. Rev. Lett. **117**, 046802 (2016).

[34] S. Kim, I. Jo, J. Nah, Z. Yao, S. K. Banerjee, and E. Tutuc, Phys. Rev. B **83**, 161401(R) (2011).

[35] J. Hu, T. Wu, J. Tian, N. N. Klimov, D. B. Newell, and Y. P. Chen, Nano Energy **40**, 42 (2017).

[36] S. Chen, Z. Han, M. M. Elahi, K. M. Masum Habib, L. Wang, B. Wen, Y. Gao, T. Taniguchi, K. Watanabe, J. Hone, A. W. Ghosh, and C. R. Dean, Science **353**, 1522 (2016).

[37] T. Mueller, F. Xia, and P. Avouris, Nat. Photonics **4**, 297 (2010).

[38] F. Xia, T. Mueller, Y. Lin, A. Valdes-Garcia, and P. Avouris, Nat. Nanotechnol. **4**, 839 (2009).

[39] J. Fang, D. Wang, C. T. DeVault, T.-F. Chung, Y. P. Chen, A. Boltasseva, V. M. Shalaev, and A. V. Kildishev, Nano Lett. **17**, 57 (2017).

[40] S. Schuler, D. Schall, D. Neumaier, L. Dobusch, O. Bethge, B. Schwarz, M. Krall, and T. Mueller, Nano Lett. **16**, 7107 (2016).

[41] X. Gan, R.-J. Shiue, Y. Gao, I. Meric, T. F. Heinz, K. Shepard, J. Hone, S. Assefa, and D. Englund, Nat. Photonics **7**, 883 (2013).

[42] Y. Yang, G. Cheng, P. Mende, I. G. Calizo, R. M. Feenstra, C. Chuang, C.-W. Liu, G. R. Jones, A. R. Hight Walker, and R. E. Elmquist, Carbon **115**, 229 (2017).

[43] A. F. Rigosi, N. R. Glavin, C.-I. Liu Y. Yang, J. Obrzut, H. M. Hill, J. Hu, H.-Y. Lee, A. R. Hight Walker, C. A. Richter, R. E. Elmquist, and D. B. Newell, Small **13**, 1700452 (2017).

[44] A. Tzalenchuk, S. Lara-Avila, A. Kalaboukhov, S. Paolillo, M. Syväjärvi, R. Yakimova, O. Kazakova, T. J. B. M. Janssen, V. Fal'ko, and S. Kubatkin, Nat Nanotechnol. **5**, 186 (2010).

[45] A. F. Rigosi, C.-I. Liu N. R. Glavin, Y. Yang, H. M. Hill, J. Hu, A. R. Hight Walker, C. A. Richter, R. E. Elmquist, and D. B. Newell, ACS Omega **2**, 2326 (2017).

[46] R. Ribeiro-Palau, F. Lafont, J. Brun-Picard, D. Kazazis, A. Michon, F. Cheynis, O. Couturaud, C. Consejo, B. Jouault, W. Poirier, and F. Schopfer, Nat. Nanotechnol. **10**, 965 (2015).

[47] T. J. B. M. Janssen, A. Tzalenchuk, R. Yakimova, S. Kubatkin, S. Lara-Avila, S. Kopylov, and V. I. Fal'ko, Phys. Rev. B **83**, 233402 (2011).

[48] Y. Fukuyama, R. E. Elmquist, L.-I. Huang, Y. Yang, F.-H. Liu, and N.-H. Kaneko, IEEE Trans. Instrum. Meas. **64**, 1451 (2015).

[49] D. A. Abanin and L. S. Levitov, Science **317**, 641 (2007).

[50] T. Lohmann, K. von Klitzing, and J. H. Smet, Nano Lett. **9**, 1973 (2009).

[51] L. Wang, I. Meric, P. Y. Huang, Q. Gao, Y. Gao, H. Tran, T. Taniguchi, K. Watanabe, L. M. Campos, D. A. Muller, J. Guo, P. Kim, J. Hone, K. L. Shepard, and C. R. Dean, Science **342**, 614 (2013).

[52] C.-H. Park, L. Yang, Y.-W. Son, M. L. Cohen, and S. G. Louie, Nat. Phys. **4**, 213 (2008).

[53] C.-H. Park, L. Yang, Y.-W. Son, M. L. Cohen, and S. G. Louie, Phys. Rev. Lett. **101**, 126804 (2008).

[54] L. Brey and H. A. Fertig, Phys. Rev. Lett. **103**, 046809 (2009).

[55] P. Burset, A. L. Yeyati, L. Brey, and H. A. Fertig, Phys. Rev. B **83**, 195434 (2011).

[56] C. W. Groth, M. Wimmer, A. R. Akhmerov, and X. Waintal, New J. Phys. **16**, 063065 (2014).

[57] Commercial equipment, instruments, and materials are identified in this paper in order to adequately specify the experimental procedure. Such identification is not intended to imply recommendation or endorsement by the National Institute of Standards and Technology or the United States government, nor is it intended to imply that the materials or equipment identified are necessarily the best available for the purpose.

[58] See Supplemental Material at http://link.aps.org/supplemental/10.1103/PhysRevB.98.045412 for sample preparation, AFM, additional setup and device images, and simulations of the 150 nm junction profile.

[59] G. Li, A. Luican, J. M. B. Lopes dos Santos, A. H. Castro Neto, A. Reina, J. Kong, and E. Y. Andrei, Nat. Phys. **6**, 109 (2010).

[60] J. R. Wallbank, A. A. Patel, M. Mucha-Kruczyński, A. K. Geim, and V. I. Fal'ko, Phys. Rev. B **87**, 245408 (2013).

[61] K. Hermann, J. Phys.: Condens. Matter **24**, 314210 (2012).